



1

2

3

4

5

6

7

8

9 **Diapycnal mixing across the photic zone of the
10 NE-Atlantic**

11

12

13

14

15

16 **by Hans van Haren*, Corina P.D. Brussaard, Loes J. A.
17 Gerringa, Mathijs H. van Manen, Rob Middag, Ruud
18 Groenewegen**

19

20

21

22

23

24

25

26

27

28

29

30

31

32

33

34

35

36

37

38

39 Royal Netherlands Institute for Sea Research (NIOZ) and Utrecht University, P.O. Box 59,
40 1790 AB Den Burg, the Netherlands.

41 *e-mail: hans.van.haren@nioz.nl

42

43



44 **Abstract.** Variable physical conditions such as vertical turbulent exchange, internal wave and
45 mesoscale eddy action, affect the availability of light and nutrients for phytoplankton
46 (unicellular algae) growth. It is hypothesized that changes in ocean temperature may affect
47 ocean vertical density stratification, which may hamper vertical exchange. In order to quantify
48 variations in physical conditions in the Northeast Atlantic Ocean, we sampled a latitudinal
49 transect along $17\pm 5^{\circ}\text{W}$ between 30°N and 62°N in summer. A shipborne Conductivity-
50 Temperature-Depth CTD-instrumented package was used with a custom-made modification of
51 the pump-inlet to minimize detrimental effects of ship motions on its data. Thorpe-scale
52 analysis was used to establish turbulence values for the upper 500 m near the surface from 3 to
53 6 profiles obtained in a short CTD-yoyo, 3 to 5 h after local sunrise. From south to north,
54 temperature decreased together with stratification while turbulence values weakly increased or
55 remained constant. Vertical turbulent nutrient fluxes across the stratification did not vary with
56 latitude. This lack of correspondence between turbulent mixing and temperature is suggested
57 to be due to internal waves breaking and acting as a potential feed-back mechanism. Our
58 findings suggest that nutrient availability for phytoplankton in the euphotic surface waters may
59 not be affected by the physical process of global warming.
60
61



62 **1 Introduction**

63 The physical environment is important for ocean life, including variations therein. For
64 example, the sun stores heat in the ocean with a stable vertical density stratification as result.
65 Generally, stratification hampers vertical turbulent exchange because of the required work
66 against (reduced) gravity before turbulence can take effect. It thus hampers a supply of nutrients
67 via a turbulent flux from deeper waters to the photic zone. However, stratification supports
68 internal waves, which (i) may move near-floating particles like phytoplankton (unicellular
69 algae) up- and down towards and away from the surface, and (ii) may induce enhanced
70 turbulence via vertical current differences (shear) resulting in internal waves breaking (Denman
71 and Gargett, 1983). Such changes in the physical environment are expected to affect the
72 availability of phytoplankton growth factors such as light and nutrients.

73 Climate models predict that global warming will reduce vertical mixing in the oceans (e.g.,
74 Sarmiento et al., 2004). Mathematical models on system stability suggest that reduced mixing
75 may generate chaotic behaviour in phytoplankton production, thereby enhancing variability in
76 carbon export into the ocean interior (Huisman et al., 2006). None of these models include
77 potential feed-back systems like internal wave action or mesoscale eddy activity. From
78 observations in the relatively shallow North Sea it is known that the strong seasonal temperature
79 stratification is marginally stable, as it supports internal waves and shear to such extent that
80 sufficient nutrients are replenished from below to sustain the late-summer bloom (van Haren et
81 al., 1999). This challenges the current paradigm in climate models.

82 In this paper, the objective is to resolve the effect of vertical stratification and turbulent
83 mixing on nutrient supply to the photic zone of the open ocean. For this purpose, upper-500-
84 m-ocean shipborne Conductivity-Temperature-Depth CTD-observations were made in
85 association with those on dissolved inorganic nutrients along a transect in the NE-Atlantic
86 Ocean from mid- to high-latitudes. This complements research based on photic zone (upper
87 100 m) observations obtained along the same transect using a slowly descending turbulence
88 microstructure profiler eight years earlier (Jurado et al., 2012). Their data demonstrated a



89 negligibly weak increase in turbulence values with decreases in stratification going north.
90 However, no nutrient data were presented and no turbulent nutrient fluxes could be computed.
91 In another study (Mojica et al., 2016), macro-nutrients and their vertical gradients were
92 presented for the upper 200 m and both found to increase from south to north. The present
93 observations go deeper to 500 m, also across the non-seasonal more permanent stratification.
94 Moreover, coinciding measurements were made of the distributions of macro-nutrients and
95 dissolved iron. This allows vertical turbulent nutrient fluxes to be computed. It leads to a
96 hypothesis concerning a physical feed-back mechanism that controls changes in stratification.

97

98 **2 Materials and Methods**

99 Between 22 July and 16 August 2017, observations were made from the R/V Pelagia in the
100 Northeast Atlantic Ocean at stations along a transect from Iceland, starting around 60°N, to the
101 Canary Islands, ending around 30°N, (Fig. 1). The transect was more or less in meridional
102 direction, with stations along 17±5°W, all in the same time zone (UTC-1 h = local time LT).
103 Full water-depth Rosette bottle water sampling was performed at most stations.

104 Samples for dissolved inorganic macro-nutrients were filtered through 0.2 µm Acrodisc
105 filter and stored frozen in a HDPE pony-vial (nitrate, nitrite and phosphate) or at 4°C (silicate)
106 until analysis. Nutrients were analysed under temperature controlled conditions using a
107 QuAAstro Gas Segmented Continuous Flow Analyser. All measurements were calibrated with
108 standards diluted in low nutrient seawater in the salinity range of the stations to ensure that
109 analysis remained within the same ionic strength. Phosphate (PO₄), nitrate plus nitrite (NO_x),
110 were measured according to Murphy and Riley (1962) and Grasshoff et al. (1983), respectively.
111 Silicate was analysed using the procedure of Strickland and Parsons (1968).

112 For dissolved iron samples the ultraclean “Pristine” sampling system for trace metals was
113 used (Rijkenberg et al., 2015). All bottles used for storage of reagents and samples were cleaned
114 according to an intensive three step cleaning protocol described by Middag et al. (2009).
115 Dissolved iron concentrations were measured shipboard using a Flow Injection—



116 Chemiluminescence method with preconcentration on iminodiaceticacid (IDA) resin as
117 described by De Baar et al. (2008) and modified by Klunder et al. (2011). In order to validate
118 the accuracy of the system, standard reference seawater (SAFe) was measured regularly in
119 triplicate (Johnson et al. 1997).

120 At 19 out of 32 stations a yoyo consisting of 3 to 6 casts of electronic CTD profiles was
121 done to monitor the temperature-salinity variability and to establish turbulent mixing values
122 from 5 to 500 m below the ocean surface. The yoyo casts were made consecutively and took
123 between 1 and 2 hours. They were mostly obtained in the morning: at ten stations between 6
124 and 8 LT, at eight stations between 8 and 10 LT, and at one station in the afternoon, around
125 noon. As the observations were made in summer, the latitudinal difference in sunrise was 1.5 h
126 between the northernmost (earlier sunrise) and southernmost stations. This difference is taken
127 into account and sampling times are referenced to time after local sunrise. It is assumed that the
128 stations sampled just after sunrise more or less reflect the upper ocean conditions of (late-)
129 nighttime cooling convection so that vertical near-homogeneity was at a maximum, and near-
130 surface stratification at a minimum, while the late morning and afternoon stations reflected
131 daytime stratifying near-surface conditions due to the stabilizing solar insolation.

132

133 **2.1 Instrumentation and modification**

134 A calibrated SeaBird 911plus CTD was used. The CTD data were processed using the
135 standard procedures incorporated in the SBE-software, including corrections for cell thermal
136 mass (Lueck, 1990) using the parameter setting of Mensah et al. (2009) and sensor time-
137 alignment. All other analyses were performed using Conservative Temperature (Θ), absolute
138 salinity SA and density anomalies σ_0 referenced to the surface using the Gibbs SeaWater-
139 software (IOC, SCOR, IAPSO, 2010).

140 Observations were made with the CTD upright rather than horizontal in a lead-weighted
141 frame without water samplers to minimize artificial turbulent overturning. Variable speeds of
142 the flow passing the temperature and conductivity sensors will cause artificial temperature and



143 thus apparent turbulent overturning, noticeable in near-homogeneous waters such as found near
144 the surface during nighttime convection. To eliminate variable flow speeds, a custom-made
145 assembly with pump in- and outlet tubes and tube-ends of exactly the same diameter was
146 mounted to the CTD as described in van Haren and Laan (2016). This reduces frictional
147 temperature effects of typically ± 0.5 mK due to fluctuations in pump speed of ± 0.5 m s⁻¹ when
148 standard SBE-tubing is used (Appendix A). The effective removal of the artificial temperature
149 effects using the custom-made assembly is demonstrated in Fig. 2, in which surface wave action
150 via ship motion is visible in the CTD-pressure record, but not in its temperature variations
151 record. For example, at station 32 the CTD was lowered in moderate sea state conditions with
152 surface waves of maximum 2 m crest-trough. The surface waves are recorded by pressure
153 variations as a result of ship motions (Fig. 2a). In the upper 40 m near the surface, the waters
154 were near-homogeneous, with temperature variations well within ± 0.5 mK (Fig. 2b). The ΔT -
155 variations did not vary with the surface wave periodicity of about 10 s. No correlation is found
156 between data in Fig. 2b and Fig. 2a. This effective removal of ship motion in CTD-temperature
157 data is confirmed for the entire 500 m depth-range in average spectral information (Fig. 2c-e).
158 In the power spectra, the pressure gradient $dp/dt \sim$ CTD-velocity shows a clear peak around 0.1
159 cps, short for cycles per s, which correspond to a period of 10 s. Such a peak is absent in both
160 spectra of temperature T and density anomaly referenced to the surface σ_0 . The correlation
161 between dp/dt and T is not significantly different from zero (Fig. 2d,e). With conventional
162 tubing and tube-ends, the surface wave variations would show in such ΔT -graph (van Haren
163 and Laan, 2016). Without the effects of ship motions, considerably less corrections need to be
164 applied for turbulence calculations (see below).

165

166 **2.2 Ocean turbulence calculation**

167 Turbulence is quantified using the analysis method by Thorpe (1977) on density (ρ)
168 inversions of less dense water below a layer of denser water in a vertical (z) profile. Such
169 inversions are interpreted as turbulent overturns of mechanical energy mixing. Vertical



170 turbulent kinetic energy dissipation rate (ε) is a measure of the amount of kinetic energy put in
171 a system for turbulent mixing. It is proportional to turbulent diapycnal flux (of density) $K_z dp/dz$.
172 In practice it is determined by calculating overturning scales with magnitude $|d|$, just like
173 turbulent eddy diffusivity (K_z). The vertical density stratification is indicated by dp/dz . The
174 turbulent overturning scales are obtained after reordering the potential density profile $\sigma_0(z)$,
175 which may contain inversions, into a stable monotonic profile $\sigma_0(z_s)$ without inversions
176 (Thorpe, 1977). After comparing raw and reordered profiles, displacements $d = \min(|z -$
177 $z_s|) \cdot \text{sgn}(z - z_s)$ are calculated that generate the stable profile. Then,

$$178 \quad \varepsilon = 0.64d^2N^3 \quad [\text{m}^2\text{s}^{-3}], \quad (1)$$

179 where $N = \{-g/\rho(dp/dz) + gp/c_s^2\}^{1/2}$ (e.g., Gill, 1982) denotes the buoyancy frequency (\sim
180 stratification squared) computed from the reordered profile. Here, g is the acceleration of
181 gravity and c_s the speed of sound reflecting pressure-compressibility effects. N is computed
182 over a typical vertical length-scale of $\Delta z = 100$ m, which more or less represents the scale of
183 large internal waves that are supported by the density stratification. The numerical constant of
184 0.64 in (1) follows from empirically relating the overturning scale magnitude with the Ozmidov
185 scale L_O of largest possible turbulent overturn in a stratified flow: $(L_O/|d|)_{\text{rms}} = 0.8$ (Dillon,
186 1982), a mean coefficient value from many realizations. Using $K_z = \Gamma \varepsilon N^2$ and a mean mixing
187 efficiency coefficient of $\Gamma = 0.2$ for the conversion of kinetic into potential energy for ocean
188 observations that are suitably averaged over all relevant turbulent overturning scales of the mix
189 of shear-, current differences, and convective, buoyancy driven, turbulent overturning in large
190 Reynolds number flow conditions (e.g., Osborn, 1980; Oakey, 1982; Ferron et al., 1998; Gregg
191 et al., 2018), we find,

$$192 \quad K_z = 0.128d^2N \quad [\text{m}^2\text{s}^{-1}]. \quad (2)$$

193 As K_z is a mechanical turbulence coefficient it is not property-dependent like a molecular
194 diffusion coefficient that is about 100-fold different for temperature compared to salinity. K_z is
195 thus the same for all turbulent transport calculations no matter what gradient of what property.
196 For example, the vertical turbulent flux of dissolved iron is computed as $K_z d(D_{\text{Fe}})/dz$.



197 According to Thorpe (1977), results from (1) and (2) are only useful after averaging over
198 the size of a turbulent overturn instead of using single displacements. Here, root-mean-square-
199 displacement values d_{rms} are not determined over individual overturns, as in Dillon (1982), but
200 over 7 m vertical intervals that just exceed average L_o . This avoids the complex distinction of
201 smaller overturns in larger ones and allows the use of a single length scale of averaging. As a
202 criterion for determining overturns we only used those data of which the absolute value of
203 difference with the local reordered value exceeds a threshold of $7 \times 10^{-5} \text{ kg m}^{-3}$, which
204 corresponds to applying a threshold of $1.4 \times 10^{-3} \text{ kg m}^{-3}$ to raw data variations (e.g., Galbraith
205 and Kelley, 1996; Stansfield et al., 2001; Gargett and Garner, 2008). Vertically averaged
206 turbulence values, short for averaged ϵ - and K_z -values from (1) and (2), can be calculated to
207 within an error of a factor of two, approximately.

208

209 **3 Results**

210 **3.1 Physical parameters**

211 An early morning vertical profile of density anomaly in the upper 500 m at a northern
212 station (Fig. 3a) is characterized by a near-homogeneous layer of about 15 to 40 m, which is
213 above a layer of relatively strong stratification and a smooth moderate stratification deeper
214 below. In the near-homogeneous upper layer, in this example $z > -30 \text{ m}$, relatively large
215 turbulent overturn displacements can be found of $d = \pm 20 \text{ m}$ (Fig. 3b): so called large density
216 inversions. For $z < -30 \text{ m}$, large turbulent overturns are few and far between. Turbulence
217 dissipation rate (Fig. 3c) and eddy diffusivity (Fig. 3d) are characterized by relatively small
218 displacement sizes of less than 5 m. For $z < -200 \text{ m}$, displacement values weakly increase with
219 depth, together with stratification ($\sim N^2$; Fig. 3e). Between $-30 < z < 0 \text{ m}$, turbulence dissipation
220 rate values between $< 10^{-11}$ and $> 10^{-8} \text{ m}^2 \text{ s}^{-3}$ are similar to those found by others, using
221 microstructure profilers (e.g., Oakey, 1982; Gregg, 1989), lowered acoustic Doppler current
222 profiler or CTD-Thorpe scale analysis (e.g., Ferron et al., 1998; Walter et al., 2005; Kunze et
223 al., 2006). Here, eddy diffusivities are found between $< 10^{-5}$ and $3 \times 10^{-3} \text{ m}^2 \text{ s}^{-1}$ and these values



224 compare with previous near-surface results (Denman and Gargett, 1983). The relatively small
225 $|d| < 5$ m displacements (Fig. 3b) are genuine turbulent overturns, and they resemble ‘Rankine
226 vortices’, a common model of cyclones (van Haren and Gostiaux, 2014), as may be best visible
227 in this example in the large turbulent overturn near the surface. The occasional erratic
228 appearance in individual profiles, sometimes still visible in the ten-profile means, reflects
229 smaller overturns in larger ones.

230 A mid-morning profile at a southern station shows different characteristics (Fig. 4),
231 although 500 m vertically averaged turbulence values are similar to within 10% of those of the
232 northern station. This 10% variation is well within the error bounds of about a factor of two. At
233 this southern station, the near-surface layer is stably stratifying (Fig. 4a) and displays few
234 overturning displacements (Fig. 4b), while the interior demonstrates rarer but occasional
235 intense turbulent overturning (at $z = -160$ m in Fig. 4), presumably due to internal wave
236 breaking. At greater depths, stratification ($\sim N^2$; Fig. 4e) weakly decreases, together with ε (Fig.
237 4c) and K_z (Fig. 4d).

238 Latitudinal overviews are given in Fig. 5 for: Average values over the upper $z > -15$ m,
239 which covers the diurnal mainly convective turbulent mixing range from the surface, average
240 values between $-100 < z < -25$ m, which covers the seasonal strong stratification, and average
241 values between $-500 < z < -100$ m, which covers the more permanent moderate stratification.
242 Noting that all panels have a vertical axis representing a logarithmic scale, variations over
243 nearly four orders of magnitude in turbulence dissipation rate (Fig. 5a) and eddy diffusivity
244 (Fig. 5b) are observed between individual average values. This variation in magnitude is
245 typically found in near-surface open-ocean turbulence microstructure profiles (e.g., Oakey,
246 1982). Still, considerable variability over about two orders of magnitude is observed between
247 the 3 to 6 cast averages at a particular station. This variation in station- and vertical averages
248 far exceeds the instrumental error bounds of a factor of two (0.3 on a log-scale), and thus reveals
249 local variability. The turbulence processes occur ‘intermittently’.

250 The observed variability over two orders of magnitude between yoyo-casts at a single
251 station may be due to active convective overturning during early morning in the near-



252 homogeneous upper layer, or due to internal wave breaking and sub-mesoscale variability
253 deeper down. Despite the large variability at stations, trend are visible between stations in the
254 upper 100 m over the 32° latitudinal range going poleward: Buoyancy frequency (~ square root
255 of stratification) steadily decreases while turbulence values remain the same or weakly increase
256 by about half an order of magnitude (about a factor of 3). The trends suggest marginally larger
257 (convective) turbulence due to larger cooling from above and larger internal wave breaking
258 going poleward. It is noted that the results are somewhat biased by the sampling scheme, which
259 changed from 3 to 4 h after sunrise sampling at high latitudes to 4 to 5 h after sunrise sampling
260 at lower latitudes, see the sampling hours after local sunrise in (Fig. 5d). Its effect is difficult to
261 quantify, but should not show up in turbulence values from deeper down ($-500 < z < -100$ m).

262 Between $-500 < z < -100$ m, no clear trend with latitude is visible in the turbulence values
263 (Fig. 5a,b), although $[K_z]$ weakly increases with increasing latitude at all levels between -500
264 $< z < 0$ m, while stratification decreases (Fig. 5c). The deeper data thus unambiguously confirm
265 the observations from the near-surface layers. Our turbulence values also confirm previous
266 results by Jurado et al. (2012) who made microstructure profiler observations from the upper z
267 > -100 m along the same transect. Their results showed turbulence values remain unchanged
268 over 30° latitude or increase by at most one order of magnitude, depending on depth level. Their
269 ‘mixed’ layer ($z > \sim -25$ m) turbulence values are similar to our $z > -15$ m values and half to one
270 order of magnitude larger than the present deeper observations. The slight discrepancy in values
271 averaged over $z > -25$ m may point at either i) a low bias due to a too strict criterion of accepting
272 density variations for reordering applied here, or ii) a high bias of the ~ 10 -m largest overturns
273 having similar velocity scales (of about 0.05 m s $^{-1}$) as their 0.1 m s $^{-1}$ slowly descending SCAMP
274 microstructure profiler. At greater depths, $-500 < z < -100$ m, it is seen in the present
275 observations that the spread in turbulence values over four orders of magnitude at a particular
276 station is also large. This spread in values suggests that dominant turbulence processes show
277 similar intermittency in weakly (at high-latitudes $N \approx 10^{2.5}$ s $^{-1}$) and moderately (at mid-latitudes
278 $N \approx 10^{2.2}$ s $^{-1}$) stratified waters, respectively, for given resolution of the instrumentation.



279 Mean values of N are larger by half an order of magnitude in the seasonal pycnocline than
280 those near the surface and in the more permanent stratification below (Fig. 5). Such local
281 vertical variations in N are the same variation as observed horizontally across latitudes [30,
282 62]° per depth level.

283

284 **3.2 Nutrient distributions and fluxes**

285 Vertical profiles of macro-nutrients generally resemble those of density anomaly in the
286 upper $z > -500$ m (Fig. 6). In the south, low macro-nutrient values are generally distributed over
287 a larger near-surface mixed layer. For $z < -100$ m below the seasonal stratification, vertical
288 gradients of macro-nutrients are large. Macro-nutrient values become more or less independent
289 of latitude at depths below $z < -500$ m. Dissolved iron profiles differ from macro-nutrient
290 profiles, notably in the upper layer near the surface. At some southern stations, dissolved iron
291 and to a lesser extent also phosphate, have relatively high concentrations closest to the surface.
292 These near-surface concentration increases suggest atmospheric sources, most likely Saharan
293 dust deposition (e.g., Rijkenberg et al., 2012).

294 As a function of latitude in the near-surface ‘mixed’ layer (Fig. 7), the vertical turbulent
295 fluxes of dissolved iron and phosphate (representing the macro-nutrients) is found constant or
296 insignificantly increasing (Fig. 7d). Here, the mean eddy diffusivity values for the near-surface
297 layer as presented in Fig. 5 are used for computing the fluxes. It is noted that in this layer
298 turbulent overturning (Figs 3b, 4b) is larger and nutrients are mainly depleted (Fig. 6), except
299 when replenished from atmospheric sources. Hereby, lateral diffusion is not considered
300 important. More interestingly, the vertical turbulent fluxes of nutrients across the seasonal
301 pycnocline (Fig. 8) are found ambiguous or statistically independently varying with latitude
302 (Fig. 8d). Likewise, the vertical turbulent fluxes of dissolved iron and phosphate are marginally
303 constant with latitude across the more permanent stratification (Fig. 9). Overall, the vertical
304 turbulent nutrient fluxes across the seasonal and more permanent stratification resemble those
305 of the physical vertical turbulent mass flux, which is equivalent to the distribution of turbulence
306 dissipation rate and which is latitude-invariant (Fig. 5a).



307

308 **4 Discussion**

309 Practically, the upright positioning CTD while using an adaptation consisting of a
310 sophisticated custom-made equal-surface inlet worked well to minimize ship-motion effects on
311 variable flow-imposed temperature variations. This improved calculated turbulence values
312 from CTD-observations in general and in near-homogeneous layers in particular. The indirect
313 comparison with previous microstructure profiler observations along the same transect (Jurado
314 et al., 2012) confirms the same trends, although occasionally turbulence values were lower (to
315 one order of magnitude in the present study). This difference in values may be due to the time
316 lapse of 8 years between the observations, but more likely it is due to inaccuracies in one or
317 both methods. It is noted that any ocean turbulence observations cannot be made better than to
318 within a factor of two (Oakey, pers. comm.). In that respect, the standard CTD with the here
319 presented adaptation is a cheaper solution than additional microstructure profiler observations.
320 Nevertheless, it would be good to perform a more extensive comparison between Thorpe scale
321 analysis data and deeper microstructure profiler data.

322 While our turbulence values are roughly similar to those of others transecting the NE-
323 Atlantic over the entire water depth (Walter et al., 2005; Kunze et al., 2006), the focus in the
324 present paper is on the upper 500 m because of its importance for upper-ocean marine biology.
325 Our study demonstrates a decrease of stratification with increasing latitude and decreasing
326 temperature that, however, does not lead to significant variation in turbulence values and
327 vertical turbulent fluxes. These findings suggest that global warming may not necessarily lead
328 to a change in vertical turbulent exchange. We hypothesize that internal waves may drive the
329 feed-back mechanism.

330 Molecular diffusivity of heat is about $10^{-7} \text{ m}^2 \text{ s}^{-1}$ in seawater, and nearly always smaller than
331 turbulent diffusivity in the ocean. The average values of K_z during our study were typically 100
332 to 1000 times larger than molecular diffusivity, which implies turbulent diapycnal mixing
333 drives vertical fluxes despite the relatively slow turbulence compared to surface wave breaking.



334 Depending on the gradient of a substance like nutrients or matter, the relatively slow turbulence
335 may not necessarily provide weak fluxes $K_z d(\text{substance})/dz$ into the photic zone. In the central
336 North Sea, a relatively low mean value of $K_z = 2 \times 10^{-5} \text{ m}^2 \text{ s}^{-1}$ comparable to values over the
337 seasonal pycnocline here, was found sufficient to supply nutrients across the strong summer
338 pycnocline to sustain the entire late-summer phytoplankton bloom in near-surface waters and
339 to warm up the near-bottom waters by some 3°C over the period of seasonal stratification (van
340 Haren et al., 1999). There, the turbulent exchange was driven by a combination of tidal currents
341 modified by the stratification, shear by inertial motions driven by the Coriolis force (inertial
342 shear) and internal wave breaking. Such drivers are known to occur in the open ocean, although
343 to unknown extent.

344 The here observed latitudinal trends of ϵ , K_z and N are more or less the same as the vertical
345 trends in these parameters at all stations. For $z < -200 \text{ m}$, turbulence values of ϵ and K_z weakly
346 vary with stratification. This is perhaps unexpected and contrary to the common belief of
347 stratification hampering vertical turbulent exchange of matter including nutrients. It is less
348 surprising when considering that increasing stratification is able to support larger shear. Known
349 sources of destabilizing shear include near-inertial internal waves of which the vertical length-
350 scale is relatively small compared to other internal waves, including internal tides (LeBlond
351 and Mysak, 1978).

352 The dominance of inertial shear over shear by internal tidal motions (internal tide shear),
353 together with larger energy in the internal tidal waves, has been observed in the open-ocean,
354 e.g. in the Irminger Sea around 60°N (van Haren, 2007). The frequent atmospheric disturbances
355 in that area generate inertial motions and dominant inertial shear. Internal tides have larger
356 amplitudes but due to much larger length scales they generate weaker shear, than inertial
357 motions. Small-scale internal waves near the buoyancy frequency are abundant and may break
358 sparsely in the ocean interior outside regions of topographic influence. However, larger
359 destabilizing shear requires larger stable stratification to attain a subtle balance of 'constant'
360 marginal stability (van Haren et al., 1999). Not only storms, but other geostrophic adjustments,
361 such as frontal collapse, may generate inertial wave shear also at low latitudes (Alford and



362 Gregg, 2001), so that overall latitudinal dependence may be negligible. If dominant, shear-
363 induced turbulence in the upper ocean may thus be latitudinally independent (Jurado et al.,
364 2012; deeper observations present study).

365 Summarizing, the vertical nutrient fluxes did not vary with latitude and stratification and
366 thus from a physical environment perspective, nutrient availability and corresponding
367 phytoplankton productivity and growth are not expected to change under future environmental
368 changes like global warming.

369

370 *Competing interests.* The authors declare that they have no conflict of interest.

371

372 *Acknowledgements.* We thank the master and crew of the R/V Pelagia for their pleasant
373 contributions to the sea-operations. J. van Heerwaarden and R. Bakker made the CTD-
374 modification.

375



376

APPENDIX A

377 **Modification of CTD pump-tubing to minimize RAM-effects**

378 The unique pump system on SeaBird Electronics (SBE) CTDs, foremost on their high-
379 precision full ocean depth shipborne and cable-lowered SBE911, minimizes the effects of flow
380 variations (and inversions) past its T-C sensors (SeaBird, 2012). This reduction in flow
381 variation is important, because the T-sensor has a slower response than the C-sensor. As data
382 from the latter are highly temperature dependent, besides being pressure dependent, the precise
383 matching of all three sensors is crucial for establishing proper salinity and density
384 measurements, especially across rapid changes in any of the parameters. As flow past the T-
385 sensor causes higher measurement values due to friction at the sensor tip, flow-fluctuations are
386 to be avoided as they create artificial T-variations of about 1 mK s m^{-1} (Larson and Pedersen,
387 1996).

388 However, while the pump itself is one thing, its tubing needs careful mounting as well, with
389 in- and outlet at the same depth level (Sea-Bird, 2012). This is to prevent ram pressure $P = \rho U^2$,
390 for density ρ and flow speed U . Unfortunately, the SBE-manual shows tubing of different
391 diameter, for in- and outlet. Different diameter tubing leads to velocity fluctuations of $\pm 0.5 \text{ m}$
392 s^{-1} past the T-sensor, as was concluded from a simple experiment by van Haren and Laan
393 (2016). The flow speed variations induce temperature variations of $\pm 0.5 \text{ mK}$ and are mainly
394 detectable in weakly stratified waters such as in the deep ocean, but also near the surface as
395 observed in the present data. Using tubes of the same diameter opening remedied most of the
396 effect, but only if the surface of the tube-opening is perpendicular to the main CT-motion as in
397 a vertically mounted CTD. If it is parallel to the main motion as in a horizontally mounted CTD,
398 the effect was found to be adverse. The make-shift onboard experiment in van Haren and Laan
399 (2016) has now been cast into a better design (Fig. A1), of which the first results are presented
400 in this paper.



401 **References**

402 Alford, M. H. and Gregg, M. C.: Near-inertial mixing: Modulation of shear, strain and
403 microstructure at low latitude, *J. Geophys. Res.*, 106, 16,947-16,968, 2001.

404 De Baar, H. J. W. et al.: Titan: A new facility for ultraclean sampling of trace elements and
405 isotopes in the deep oceans in the international Geotraces program, *Mar. Chem.*, 111, 4-21,
406 2008.

407 Denman, K. L. and Gargett, A. E.: Time and space scales of vertical mixing and advection of
408 phytoplankton in the upper ocean, *Limnol. Oceanogr.*, 28, 801-815, 1983.

409 Dillon, T. M.: Vertical overturns: A comparison of Thorpe and Ozmidov length scales, *J.*
410 *Geophys. Res.*, 87, 9601-9613, 1982.

411 Ferron, B., Mercier, H., Speer, K., Gargett, A. and Polzin, K.: Mixing in the Romanche Fracture
412 Zone, *J. Phys. Oceanogr.*, 28, 1929-1945, 1998.

413 Galbraith, P. S. and Kelley, D. E.: Identifying overturns in CTD profiles, *J. Atmos. Oc.*
414 *Technol.*, 13, 688-702, 1996.

415 Gargett, A. and Garner, T.: Determining Thorpe scales from ship-lowered CTD density
416 profiles, *J. Atmos. Oc. Technol.*, 25, 1657-1670, 2008.

417 Gill, A. E.: *Atmosphere-Ocean Dynamics*, Academic Press, Orlando, Fl, USA, 662 pp, 1982.

418 Grasshoff, K., Kremling, K. and Ehrhardt, M.: *Methods of seawater analysis*, Verlag
419 Chemie GmbH, Weinheim, 419 pp, 1983.

420 Gregg, M. C.: Scaling turbulent dissipation in the thermocline, *J. Geophys. Res.*, 94, 9686-
421 9698, 1989.

422 Gregg, M. C., D'Asaro, E. A., Riley, J. J. and Kunze, E.: Mixing efficiency in the ocean, *Ann.*
423 *Rev. Mar. Sci.*, 10, 443-473, 2018.

424 Huisman, J., Pham Thi, N. N., Karl, D. M. and Sommeijer, B.: Reduced mixing generates
425 oscillations and chaos in the oceanic deep chlorophyll maximum, *Nature*, 439, 322-325,
426 2006.



427 Jurado, E., van der Woerd, H. J. and Dijkstra, H. A.: Microstructure measurements along a
428 quasi-meridional transect in the northeastern Atlantic Ocean, *J. Geophys. Res.*, 117,
429 C04016, doi:10.1029/2011JC07137, 2012.

430 IOC, SCOR, IAPSO: The international thermodynamic equation of seawater – 2010:
431 Calculation and use of thermodynamic properties, Intergovernmental Oceanographic
432 Commission, Manuals and Guides No. 56, UNESCO, Paris, France, 196 pp, 2010.

433 Johnson, K. S., Gordon, R. M. and Coale, K. H.: What controls dissolved iron concentrations
434 in the world ocean? *Mar. Chem.*, 57, 137-161, 1997.

435 Klunder, M. B., Laan, P., Middag, R., De Baar, H. J. W. and van Ooijen, J. C.: Dissolved iron
436 in the Southern Ocean (Atlantic sector), *Deep-Sea Res. II*, 58, 2678-2694, 2011.

437 Kunze, E., Firing, E., Hummon, J. M., Chereskin, T. K. and Thurnherr, A. M.: Global
438 abyssal mixing inferred from lowered ADCP shear and CTD strain profiles, *J. Phys.*
439 *Oceanogr.* 36, 1553-1576, 2006.

440 Larson, N., Pedersen, A. M.: Temperature measurements in flowing water: viscous heating
441 of sensor tips, *Proc. 1st IGHEM Meeting*, Montreal, PQ, Canada. [Available online at
442 http://www.seabird.com/technical_references/viscous.htm], 1996.

443 LeBlond, P. H. and Mysak, L. A.: Waves in the Ocean, Elsevier, Amsterdam NL, 602 pp, 1978.

444 Lueck, R. G.: Thermal inertia of conductivity cells: Theory, *J. Atmos. Oc. Technol.*, 7, 741-
445 755, 1990.

446 Mensah, V., Le Menn, M. and Morel, Y.: Thermal mass correction for the evaluation of salinity,
447 *J. Atmos. Oc. Tech.*, 26, 665-672, 2009.

448 Middag, R., de Baar, H. J. W., Laan, P. and Bakker, K.: Dissolved aluminium and the silicon
449 cycle in the Arctic Ocean, *Marine Chemistry*, 115, 176-195, 2009.

450 Mojica, K. D. A., Huisman, J., Wilhelm, S. W. and Brussaard, C. P. D.: Latitudinal variation
451 in virus-induced mortality of phytoplankton across the North Atlantic Ocean, *ISME J.*, 10,
452 500-513, 2016.



453 Murphy, J. and Riley, J. P.: A modified single solution method for the determination of
454 phosphate in natural waters, *Anal. Chim. Acta*, 27, 31-36, 1962.

455 Oakey, N. S.: Determination of the rate of dissipation of turbulent energy from simultaneous
456 temperature and velocity shear microstructure measurements, *J. Phys. Oceanogr.*, 12, 256-
457 271, 1982.

458 Osborn, T. R.: Estimates of the local rate of vertical diffusion from dissipation measurements,
459 *J. Phys. Oceanogr.*, 10, 83-89, 1980.

460 Rijkenberg, M. J. A. et al.: Fluxes and distribution of dissolved iron in the eastern (sub-) tropical
461 North Atlantic Ocean, *Glob. Biogeochem. Cycl.*, 26, GB3004,
462 doi:10.1029/2011GB004264, 2012.

463 Rijkenberg, M. J. A. et al.: "PRISTINE", a new high volume sampler for ultraclean sampling
464 of trace metals and isotopes, *Mar. Chem.*, 177, 501-509, 2015.

465 Sarmiento, J. L. et al.: Response of ocean ecosystems to climate warming, *Glob. Biogeochem.*
466 *Cycl.*, 18, doi:10.1029/2003GB002134, 2004.

467 Sea-Bird: Fundamentals of the TC duct and pump-controlled flow used on Sea-Bird CTDs,
468 *Proc. Sea-Bird Electronics Appl. note* 38, SBE, Bellevue, WA, USA, 5 pp, 2012.

469 Smith, W. H. F. and Sandwell, D. T. : Global seafloor topography from satellite altimetry and
470 ship depth soundings, *Science* 277, 1957-1962, 1997.

471 Stansfield, K., Garrett, C., Dewey, R.: The probability distribution of the Thorpe displacement
472 within overturns in Juan de Fuca Strait, *J. Phys. Oceanogr.*, 31, 3421-3434, 2001.

473 Strickland, J. D. H. and Parsons, T. R.: A practical handbook of seawater analysis, First
474 edition, *Fisheries Research Board of Canada, Bulletin*, 167, 293 pp, 1968.

475 Thorpe, S. A.: Turbulence and mixing in a Scottish loch, *Phil. Trans. Roy. Soc. Lond. A*, 286,
476 125-181, 1977.

477 van Haren, H.: Inertial and tidal shear variability above Reykjanes Ridge, *Deep-Sea Res. I*, 54,
478 856-870, 2007.



479 van Haren, H. and Gostiaux, L.: Characterizing turbulent overturns in CTD-data, *Dyn. Atmos.*
480 *Oc.*, 66, 58-76, 2014.

481 van Haren, H. and Laan, M.: An in-situ experiment identifying flow effects on temperature
482 measurements using a pumped CTD in weakly stratified waters, *Deep-Sea Res. I*, 111, 11-
483 15, 2016.

484 van Haren, H., Maas, L., Zimmerman, J. T. F., Ridderinkhof, H. and Malschaert, H.: Strong
485 inertial currents and marginal internal wave stability in the central North Sea, *Geophys.*
486 *Res. Lett.*, 26, 2993-2996, 1999.

487 Walter, M., Mertens, C. and Rhein, M.: Mixing estimates from a large-scale hydrographic
488 survey in the North Atlantic, *Geophys. Res. Lett.*, 32, L13605, doi:10.1029/2005GL022471,
489 2005.

490



491 **Figure 1.** Bathymetry map of the Northeast Atlantic Ocean based on the 9.1 ETOPO-1 version
492 of satellite altimetry-derived data by Smith and Sandwell (1997). The numbered circles
493 indicate the CTD stations. Depth contours are at 2500 and 5000 m.

494

495 **Figure 2.** Test of effective removal of ship motions in CTD-data after pump in- and outlet
496 modification. Nearly raw 24 Hz sampled downcast data obtained from northern station 32
497 (cast 9). Short example time series for the 20-m depth range [10, 30] m. (a) Detrended
498 pressure (blue) and its (negative signed) first time derivative $-dp/dt$, 2-dbar-smoothed
499 (purple). (b) Detrended temperature. (c) Moderately smoothed (~30 degrees of freedom;
500 dof) spectra of data from the 5 to 500 m depth range. (d) Moderately smoothed (40 dof)
501 coherence between dp/dt and T from c., with dashed line indicating the 95% significance
502 level. (e) Corresponding phase difference.

503

504 **Figure 3.** Upper 500 m of turbulence characteristics computed from downcast density anomaly
505 data applying a threshold of $7 \times 10^{-5} \text{ kg m}^{-3}$. Northern station 29, cast 2. (a) Unordered, ‘raw’
506 profile of density anomaly referenced to the surface. (b) Overturn displacements following
507 reordering of the profiles in a. Slopes $\frac{1}{2}$ (solid lines) and 1 (dashed lines) are indicated. (c)
508 Logarithm of dissipation rate computed from the profiles in a., averaged over 7 m intervals.
509 (d) As c., but for eddy diffusivity. (e) Logarithm of buoyancy frequency computed after
510 reordering the profiles of a.

511

512 **Figure 4.** As Fig. 3, but for a southern station. Upper 500 m of turbulence characteristics
513 computed from downcast density anomaly data applying a threshold of $7 \times 10^{-5} \text{ kg m}^{-3}$.
514 Southern station 3, cast 4. (a) Unordered, ‘raw’ profile of density anomaly referenced to
515 the surface. (b) Overturn displacements following reordering of the profiles in a. Slopes $\frac{1}{2}$
516 (solid lines) and 1 (dashed lines) are indicated. (c) Logarithm of dissipation rate computed
517 from the profiles in a., averaged over 7 m intervals. (d) As c., but for eddy diffusivity. (e)
518 Logarithm of buoyancy frequency computed after reordering the profiles of a.



519

520 **Figure 5.** Summer 2017 latitudinal transect along $17\pm 5^\circ\text{W}$ of turbulence values for upper 15 m
521 averages (green) and averages between $-100 < z < -25$ m (blue, seasonal pycnocline) and -
522 $500 < z < -100$ m (black, more permanent pycnocline) from short yoyos of 3 to 6 CTD-
523 casts. Values are given per cast (o) and station average (heavy circle with x; the size
524 corresponds with \pm the standard error for turbulence parameters). (a) Logarithm of
525 dissipation rate. (b) Logarithm of diffusivity. (c) Logarithm of buoyancy frequency (the
526 small symbols have the size of \pm the standard error). (d) Hour of sampling after sunrise.

527

528 **Figure 6.** Upper 500 m profiles for stations at three latitudes. (a) Density anomaly referenced
529 to the surface, including profiles from Fig. 3a and 4a. (b) Nitrate plus nitrite. (c) Phosphate.
530 (d) Silicate. (e) Dissolved iron.

531

532 **Figure 7.** Latitudinal transect of near-surface nutrient concentrations. (a) Dissolved iron. (b)
533 Nitrate plus nitrite (red) and phosphate (blue, scale times 10). (c) Logarithm of vertical
534 gradients of values dissolved iron in a. and phosphate in b. (d). Vertical turbulent fluxes of
535 concentrations in c. using average surface K_z from Fig. 5c.

536

537 **Figure 8.** As Fig. 7, but for $-100 < z < -25$ m.

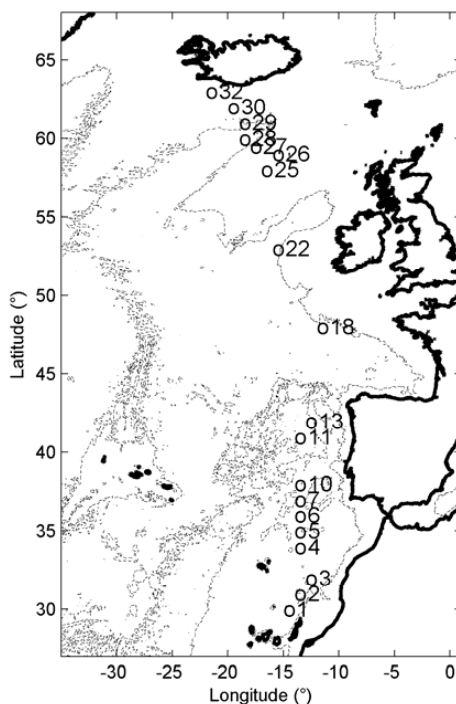
538

539 **Figure 9.** As Fig. 7, but for $-600 < z < -100$ m.

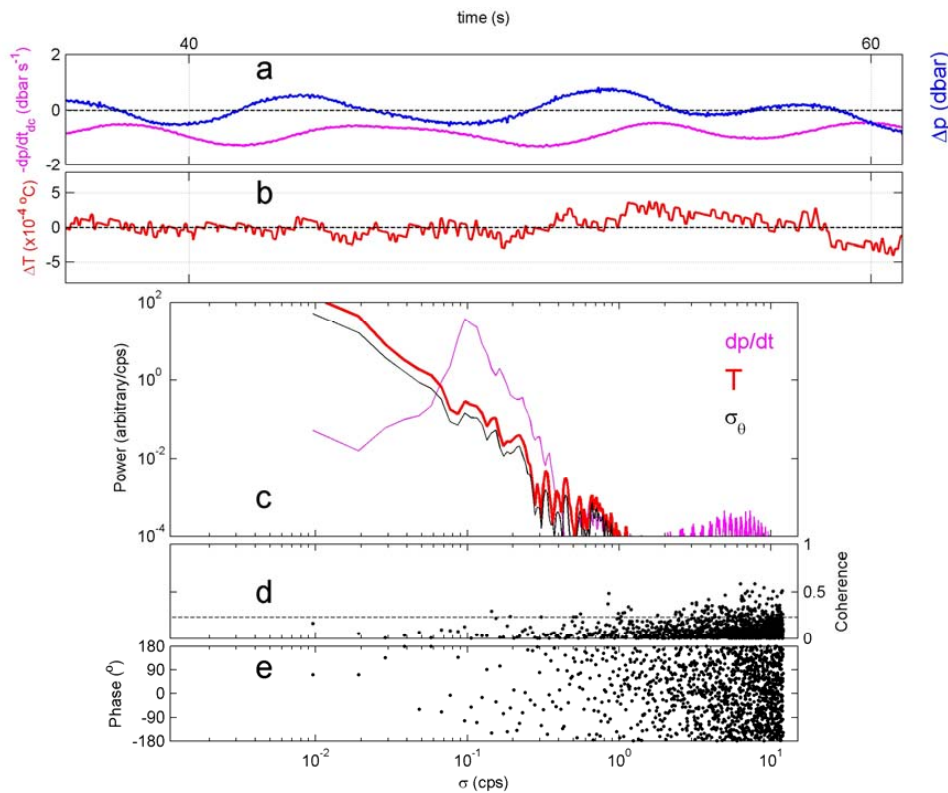
540

541 **Fig. A1.** SBE911 CTD-pump in- and outlet modification following the findings in van Haren
542 and Laan (2016). (a) The T- and C-sensors clamped together with a structure holding in-
543 and outlet pump-tubing of exactly the same diameter, separated at 0.3 m distance in the
544 horizontal plane. (b) The modification of a. mounted in the CTD-frame.

545

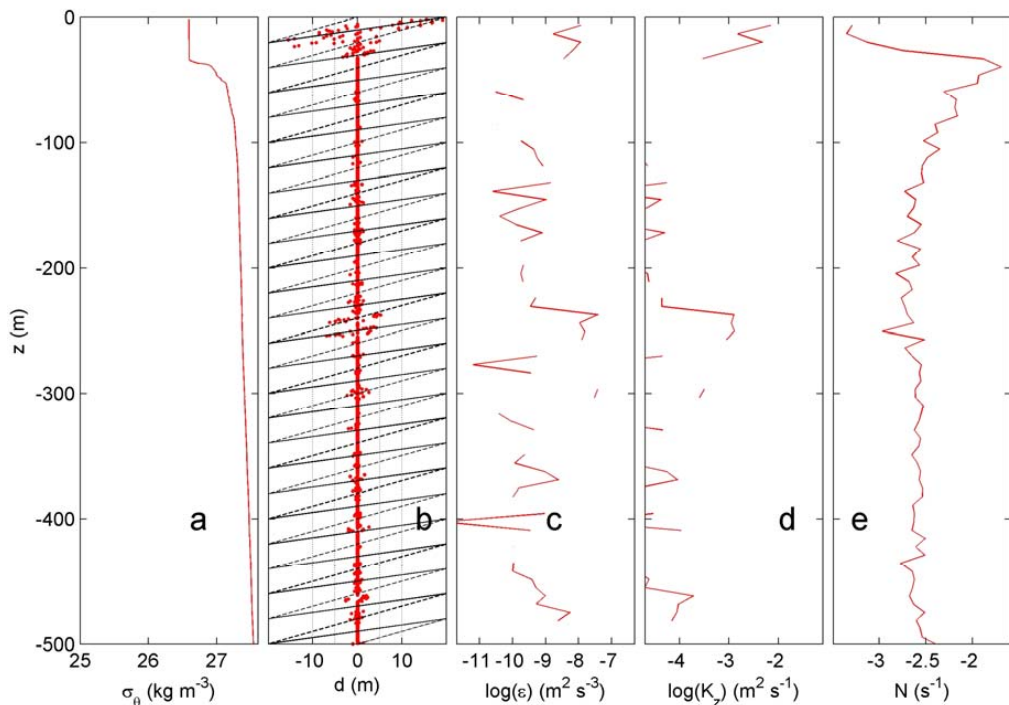


546
547 **Figure 1.** Bathymetry map of the Northeast Atlantic Ocean based on the 9.1 ETOPO-1
548 version of satellite altimetry-derived data by Smith and Sandwell (1997). The numbered
549 stations indicate the CTD stations. Depth contours are at 2500 and 5000 m.
550

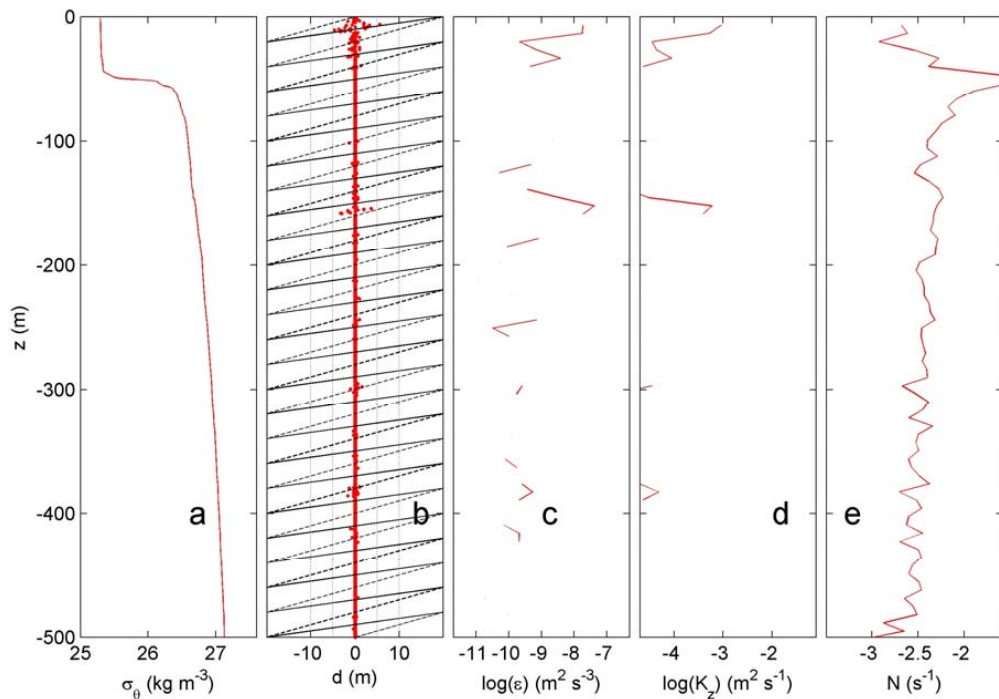


551
552
553
554
555
556
557
558
559
560

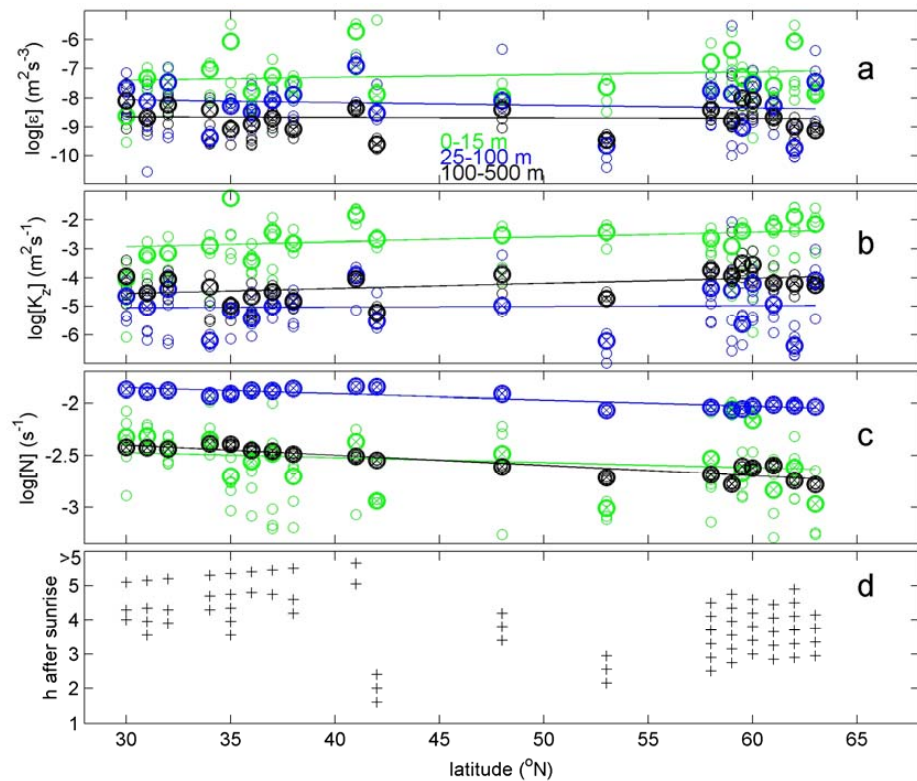
Figure 2. Test of effective removal of ship motions in CTD-data after pump in- and outlet modification. Nearly raw 24 Hz sampled downcast data obtained from northern station 32 (cast 9). Short example time series for the 20-m depth range [10, 30] m. (a) Detrended pressure (blue) and its (negative signed) first time derivative $-dp/dt$, 2-dbar-smoothed (purple). (b) Detrended temperature. (c) Moderately smoothed (~30 degrees of freedom; dof) spectra of data from the 5 to 500 m depth range. (d) Moderately smoothed (40 dof) coherence between dp/dt and T from c., with dashed line indicating the 95% significance level. (e) Corresponding phase difference.



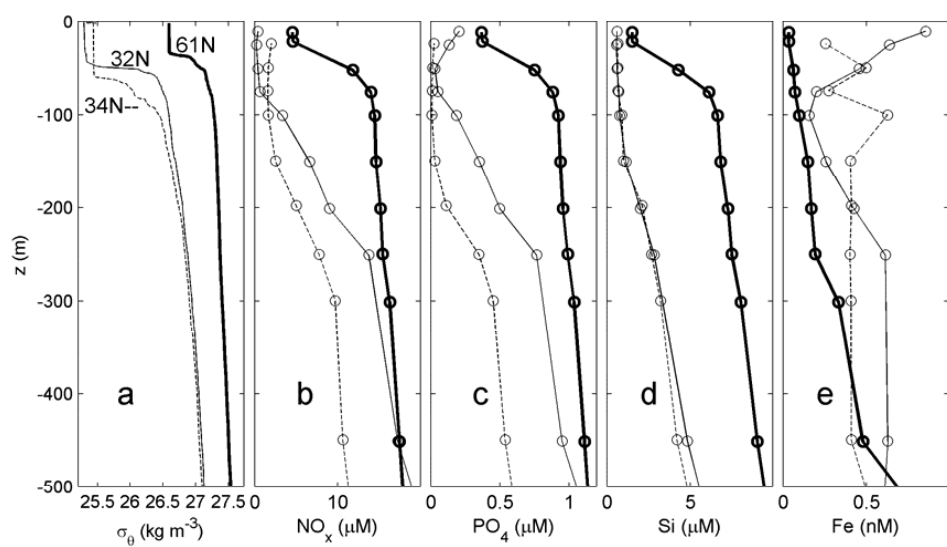
561
562 **Figure 3.** Upper 500 m of turbulence characteristics computed from downcast density
563 anomaly data applying a threshold of $7 \times 10^{-5} \text{ kg m}^{-3}$. Northern station 29, cast 2. (a)
564 Unordered, 'raw' profile of density anomaly referenced to the surface. (b) Overturn
565 displacements following reordering of the profiles in a. Slopes $1/2$ (solid lines) and 1
566 (dashed lines) are indicated. (c) Logarithm of dissipation rate computed from the profiles
567 in a., averaged over 7 m intervals. (d) As c., but for eddy diffusivity. (e) Logarithm of
568 buoyancy frequency computed after reordering the profiles of a.
569



570
571 **Figure 4.** As Fig. 3, but for a southern station. Upper 500 m of turbulence characteristics
572 computed from downcast density anomaly data applying a threshold of $7 \times 10^{-5} \text{ kg m}^{-3}$.
573 Southern station 3, cast 4. (a) Unordered, ‘raw’ profile of density anomaly referenced to
574 the surface. (b) Overturn displacements following reordering of the profiles in a. Slopes $\frac{1}{2}$
575 (solid lines) and 1 (dashed lines) are indicated. (c) Logarithm of dissipation rate computed
576 from the profiles in a., averaged over 7 m intervals. (d) As c., but for eddy diffusivity. (e)
577 Logarithm of buoyancy frequency computed after reordering the profiles of a.
578

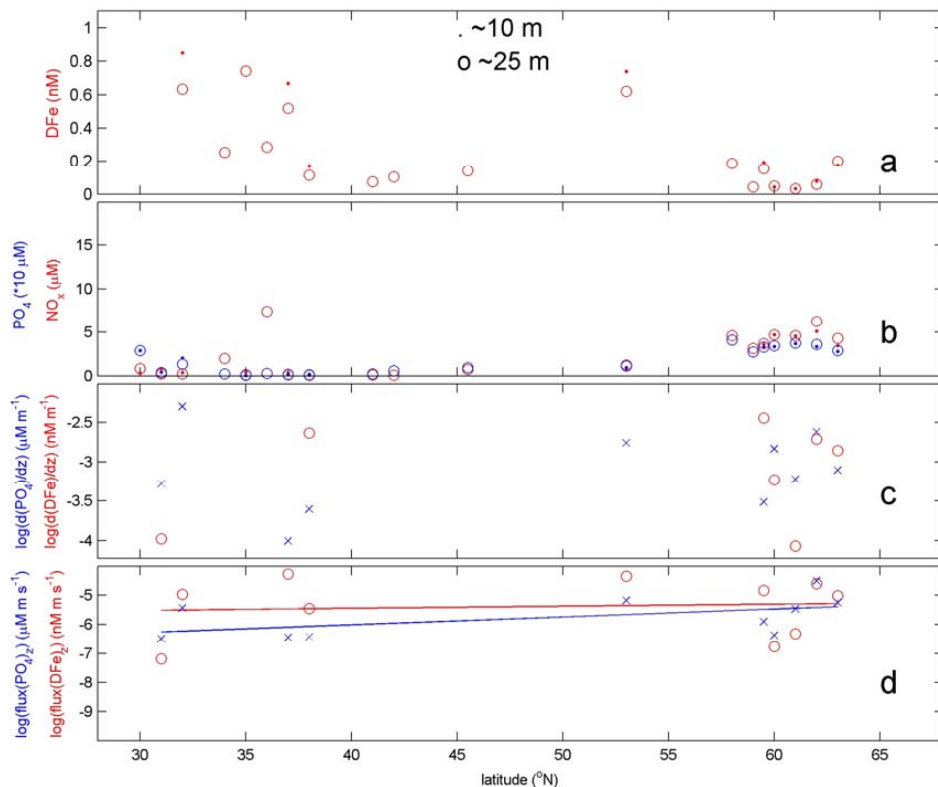


579
580 **Figure 5.** Summer 2017 latitudinal transect along $17\pm 5^\circ\text{W}$ of turbulence values for upper
581 15 m averages (green) and averages between $-100 < z < -25$ m (blue, seasonal pycnocline)
582 and $-500 < z < -100$ m (black, more permanent pycnocline) from short yoyos of 3 to 6
583 CTD-casts. Values are given per cast (o) and station average (heavy circle with x; the size
584 corresponds with \pm the standard error for turbulence parameters). (a) Logarithm of
585 dissipation rate. (b) Logarithm of diffusivity. (c) Logarithm of buoyancy frequency (the
586 small symbols have the size of $\pm a$ standard error). (d) Hour of sampling after sunrise.
587



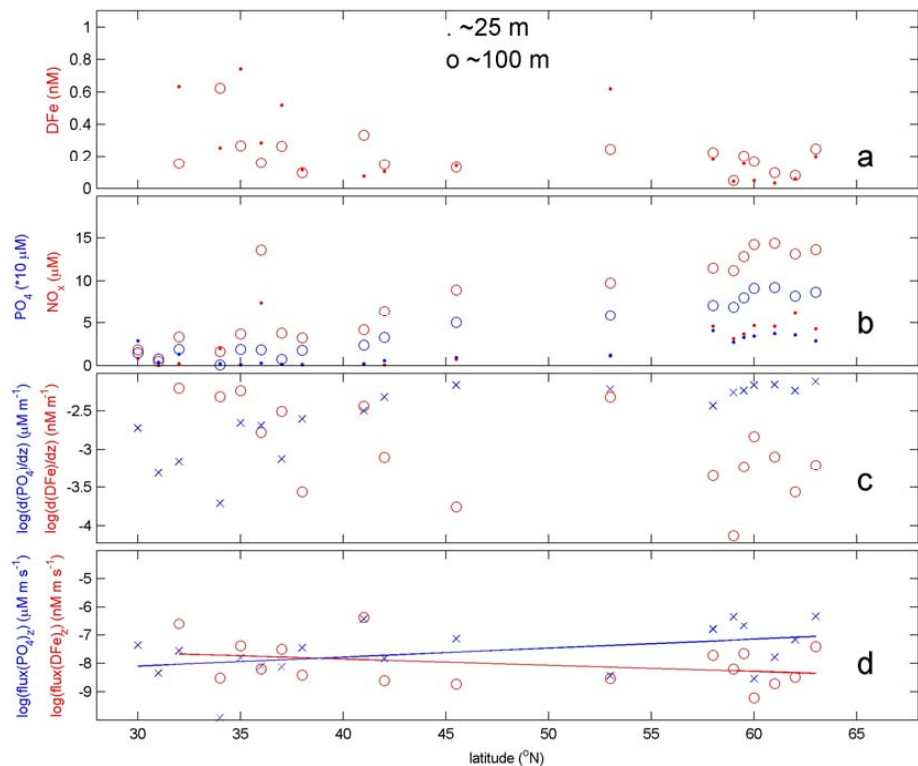
588
589
590
591
592

Figure 6. Upper 500 m profiles for stations at three latitudes. (a) Density anomaly referenced to the surface, including profiles from Fig. 3a and 4a. (b) Nitrate plus nitrite. (c) Phosphate. (d) Silicate. (e) Dissolved iron.



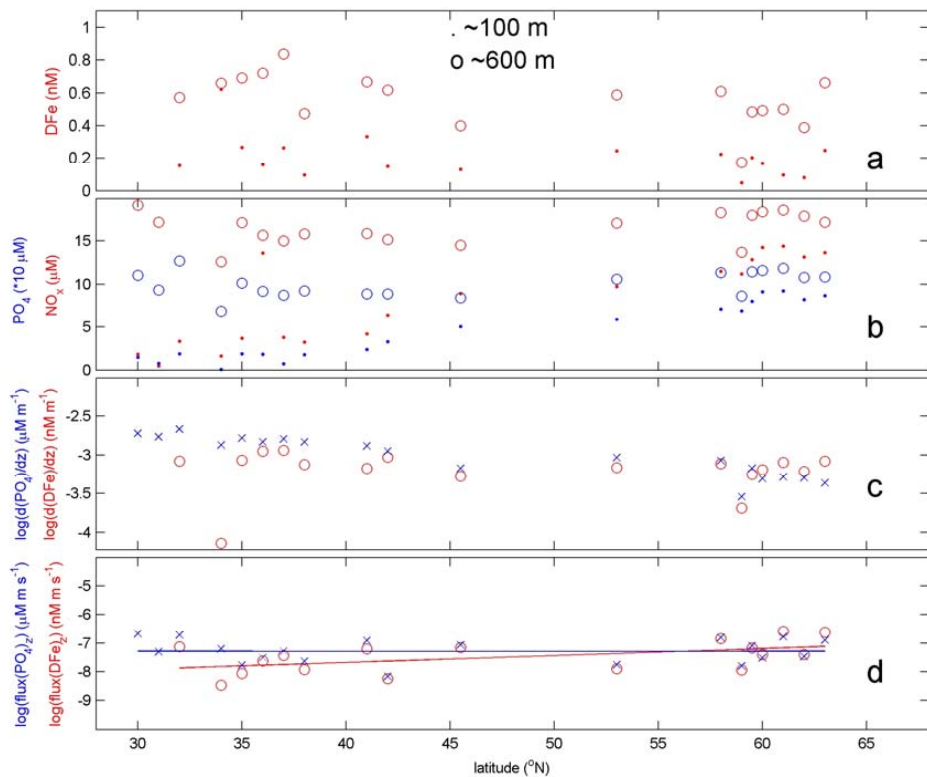
593
594
595
596
597
598

Figure 7. Latitudinal transect of near-surface nutrient concentrations. (a) Dissolved iron. (b) Nitrate plus nitrite (red) and phosphate (blue, scale times 10). (c) Logarithm of vertical gradients of values dissolved iron in a. and phosphate in b. (d) Vertical turbulent fluxes of concentrations in c. using average surface K_z from Fig. 5c.

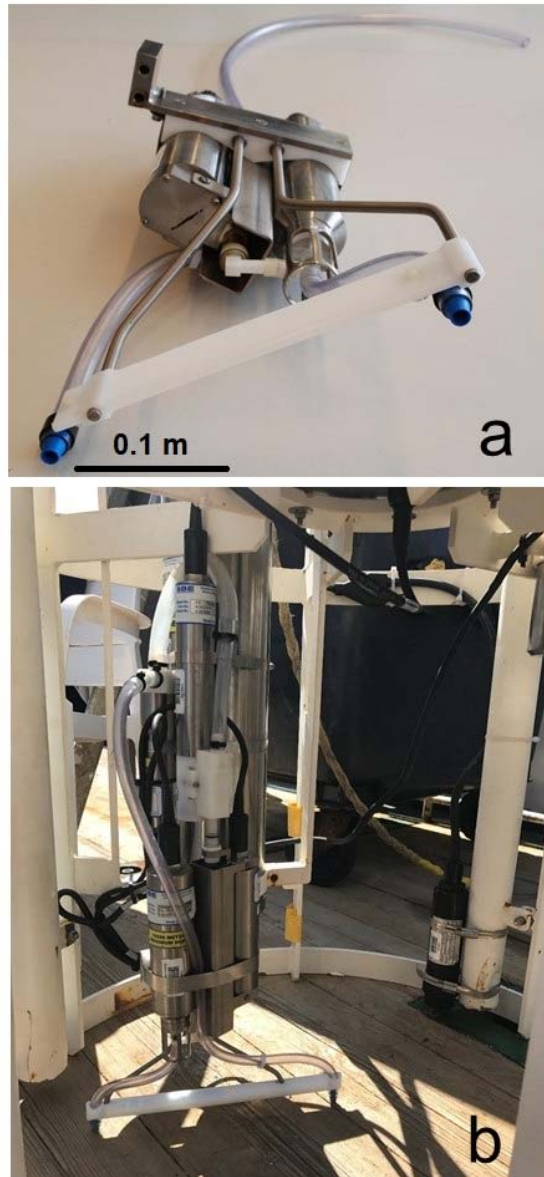


599
600
601

Figure 8. As Fig. 7, but for $-100 < z < -25$ m.



602
603 **Figure 9.** As Fig. 7, but for -600 (few nutrients sampled at 500) < z < -100 m.
604



605
606
607
608
609
610

Fig. A1. SBE911 CTD-pump in- and outlet modification following the findings in van Haren and Laan (2016). (a) The T- and C-sensors clamped together with a structure holding in- and outlet pump-tubing of exactly the same diameter, separated at 0.3 m distance in the horizontal plane. (b) The modification of a. mounted in the CTD-frame.